Medicine in Novel Technology and Devices 15 (2022) 100134

Contents lists available at ScienceDirect

Medicine in Novel Technology and Devices

journal homepage: www.journals.elsevier.com/medicine-in-novel-technology-and-devices/

Full Length Article

Optical coherence elastography of 3D bilayer soft solids using full-field and partial displacement measurements

Dongmei Zhao [a,b], Haosen Wang [e], Jianwei Deng [a,b], Iryna Slavashevich [f], Xu Guo [a,b,c], Yue Mei [a,b,c,d,*], Cuiru Sun [e,**]

[a] State Key Laboratory of Structural Analysis for Industrial Equipment, Department of Engineering Mechanics, Dalian University of Technology, Dalian 116023, PR China
[b] International Research Center for Computational Mechanics, Dalian University of Technology, PR China
[c] Ningbo Institute of Dalian University of Technology, Ningbo, China
[d] DUT-BSU Joint Institute, Dalian University of Technology, 116023, PR China
[e] Department of Mechanics, Tianjin University, 300354, PR China
[f] Bio and Nanomechanics Department, Belarusian State University, 220030, Minsk, Belarus

ARTICLE INFO

Keywords:
Inverse problem
Bilayer solid
Shear modulus distribution
Optical coherence elastography (OCE)

ABSTRACT

Characterizing nonhomogeneous elastic property distribution of soft tissues plays a crucial role in disease diagnosis and treatment. In this paper, we will apply the optical coherence elastography to reconstruct the shear modulus elastic property distribution of a bilayer solid. In the computational aspect, we adopt a well-established inverse technique that solves for every nodal shear modulus in the problem domain (NO method). Additionally, we also propose a novel inverse method that assumes the shear moduli merely vary along the thickness of the bilayer solid (TO method). The inversion tests using simulated data demonstrate that TO method performs better in reconstructing the shear modulus distribution. Further, we utilize the experimental data obtained from the optical coherence tomography to reconstruct the shear modulus distribution of a bilayer phantom. We observe that the quality of the reconstructed shear modulus distribution obtained by the partial displacement measurement is better than that obtained by the full-field displacement measurement. Particularly, merely using the displacement component along the loading direction significantly improves the reconstructed results. This work is of great significance in applying optical coherence elastography (OCE) to characterize the elastic property distribution of layered soft tissues such as skins and corneas.

1. Introduction

Characterization of spatially-varying elastic properties distribution of biological tissues plays a significant role in biomedical engineering and clinical medicine [1,2]. For instance, lumps is usually about 5–10 times stiffer than the normal tissue [3]; the shear modulus value of cribriform plate in patients with glaucoma was higher than that in healthy people [4]; the valve leaflets become stiffer during calcification [5]. Therefore, identifying the nonhomogeneous material property distribution of biological tissue is of great significance in disease diagnosis and treatment.

In order to obtain the nonhomogeneous material parameter distribution of soft tissues, the imaging facilities should be combined with inverse algorithms. That is, the imaging facilities including but not limited to ultrasound technology [6], magnetic resonance imaging (MRI) [7], optical coherence tomography (OCT) [8–10], are used to measure the displacement field of the soft tissue. The acquired measured displacement field is subsequently utilized to solve the inverse problem in elasticity so as to reconstruct the nonhomogeneous elastic property distribution of soft tissues. Since reconstructing the nonhomogeneous elastic property distribution of solids requires to solve a large-scale optimization problem, a typical way to solve the inverse problem of elasticity with high efficacy is the optimization scheme with the adjoint method [11]. This adjoint based optimization method has been used to identify the nonhomogeneous linear elastic [12], hyperelastic [13], and viscoelastic property distributions [14] of soft solids.

Usually, the nonhomogeneous elastic property distribution of solids is

* Corresponding author. State Key Laboratory of Structural Analysis for Industrial Equipment, Department of Engineering Mechanics, Dalian University of Technology, Dalian, 116023, PR China.
** Corresponding author.
E-mail addresses: meiyue@dlut.edu.cn (Y. Mei), carry_sun@tju.edu.cn (C. Sun).

https://doi.org/10.1016/j.mednotd.2022.100134
Received 29 December 2021; Received in revised form 31 March 2022; Accepted 10 April 2022

acquired using the full-field displacement measurement. However, in practice, even the state of art imaging techniques cannot guarantee that the displacement measurement is accurate everywhere in the domain of interest. Thus, whether it is possible to reconstruct elastic property distribution with high accuracy merely using partial data remains an open question.

Compared to other imaging modalities, OCT can provide fast non-inverse measurement with high resolution [15]. To this end, this paper will utilize the optical coherence elastography (OCE) to characterize a bilayer tissue mimicking phantom with full-field and partial displacement measurements. In the **Method** section, we will discuss the experimental and computational aspects of OCE. In the **Results** section, we will present the reconstruction results obtained by both synthetic data and experimental displacement measurement. The observations in **Results** sections are thoroughly discussed in the **Discussion** section. Finally, the **Conclusion** section will summarize this work.

2. Method

The general framework of the proposed method to identify the spatial variation of the shear modulus distribution of soft solids is shown in Fig. 1. Firstly, we measure the displacement field of a bilayer soft solids with OCT. Subsequently, the measured displacement field is used to solve the inverse problem in elasticity to characterize the nonhomogeneous elastic property distribution of the bilayer solid.

2.1. Experiments

An OCT system was used to measure the three-dimensional (3D) displacements of a bi-layer phantom under compression. The OCT system consists of a swept source OCT imaging system and a compressive loading device. The laser emitted from the scanning laser source (HSL-20-100-B, Santec, Aichi, Japan) interferes after splitting. The balance detector (EBR370006-02, Exalos, Schlieren, Switzerland) converts the interference signals of the two beams into electrical signals and transmits them to the acquisition card (U5303A, Germany technology, Switzerland). A photo of the loading device with the OCT scanning lens is shown in Fig. 2(a). The central wavelength of OCT is 1315 nm; the bandwidth is 88 nm and the axial resolution is 7.09 μm in tissue. The lateral resolution of the OCT system is 18.7 μm. The penetration depth to the soft solids is about 2 mm. The compressive loading device consists of an optical window to deform the specimen and allow the OCT light to pass through. A force sensor was set on the base of the loading device to measure the applied load as shown in Fig. 2(a). The top layer of the phantom was made by mixing 1 μm and 0.5 mg/mL TiO_2 scatters with 0-degree silica gel, and the bottom layer was mixed with 15-degree silica gel. The preparation of silica gel experimental sample and the selection of calculation area can ensure the flatness of surface leveler, and the sample can be regarded as isotropic material. Young's moduli of each layer was 120.8 kPa and 426.1 kPa by tensile tests. The dimensions of the double-layer phantom were 4.20mm × 4.00mm × 1.90 mm. During the exper-

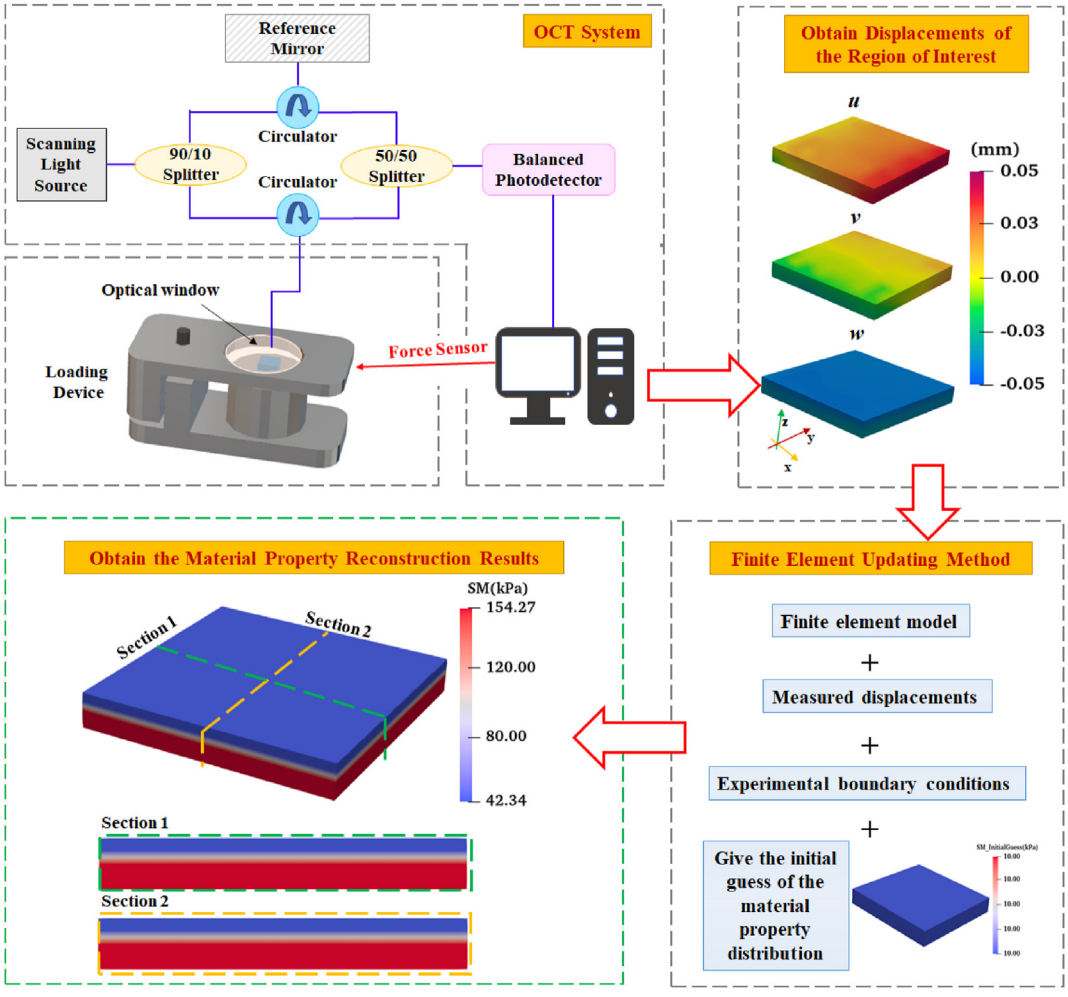

Fig. 1. The general framework of the proposed OCE method.

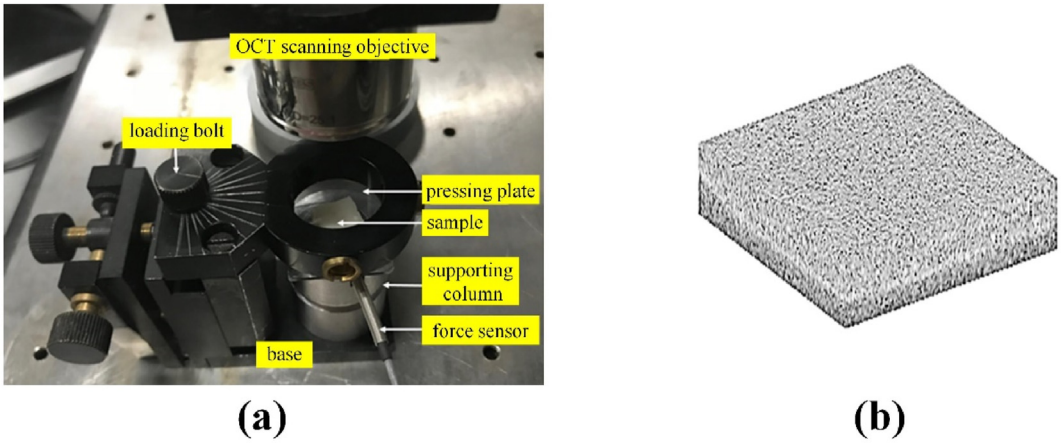

Fig. 2. (a) A photo of the loading device and the OCT scanning lens of the OCE system; (b) a 3D OCT image of a bi-layer phantom.

iment, the phantom was preloaded for 1.320 N, then compressed by 0.247 N. Two volumetric OCT images were obtained before and after compression. One of the images is shown in Fig. 2(b). Then a volume of interest(VOI) of $Lx = Ly = 2.8611$ mm and $Lz = 0.3972$ mm were selected to perform digital volume correlation(DVC). Full-field 3D displacements of the VOI were then obtained. Details about the experimental setup and the measurement procedure can be found in Ref. [10].

2.2. Inverse algorithm

2.2.1. Forward problem

The forward problem in linear elasticity is stated as follows:

$$\begin{aligned} \nabla \cdot \boldsymbol{\sigma} &= 0 \quad \text{on} \quad \Omega \\ u &= u' \quad \text{on} \quad \Gamma_u \\ \boldsymbol{\sigma} \cdot n &= t' \quad \text{on} \quad \Gamma_\sigma \end{aligned} \tag{1}$$

where ∇ denotes the divergence operator; $\mathbf{u}$ and $\boldsymbol{\sigma}$ are the displacement vector and Cauchy stress tensor, respectively. Ω is the problem domain of interest. $\mathbf{u}'$ is the prescribed displacement on the displacement boundary Γ_u, $\mathbf{t}'$ is the prescribed traction on the traction boundary Γ_σ. The relationships between traction and displacement boundaries are $\Gamma_u \cup \Gamma_\sigma = \partial\Omega$ and $\Gamma_u \cap \Gamma_\sigma = \varnothing$. We also assume the soft solid obeys incompressible and linear elastic law where shear modulus is the only material property in the stress-strain relation.

2.2.2. Inverse problem

Characterizing elastic property distribution of solids can be considered as a constrained optimization problem. With the acquired measured displacement fields, the objective function can be written as:

$$J = \frac{1}{2}\int_\Omega (u - u_{\text{meas}})^2 d\Omega + \frac{\alpha}{2}\int_\Omega \sqrt{(\nabla\mu)^2 + c_0{}^2}\ d\Omega \tag{2}$$

where $\mathbf{u}$ and $\mathbf{u}_{\text{meas}}$ are computed displacement field obtained by the finite element simulation and measured displacement field, respectively. α is the regularization factor which controls the weight of the regularization term (the second term in the objective function) [16]. μ denotes the unknown shear modulus. $c_0 = 0.01$ is a small constant, which avoids the singularity issue when calculating the gradient of the objective function with respect to shear moduli.

In this paper, the limited Broyden-Fletcher-Goldfarb-Shanno(L-BFGS) method [17] is utilized to solve the constrained optimization problem. L-BFGS method is a gradient-based method, and we need to calculate the gradient of the objective function with respect to every optimization variable in each minimization iteration. Thus, it is computationally expensive for calculating gradients for a large-scale optimization problem. To address this issue, we will utilize the adjoint method to compute the spatial gradients of the objective function efficiently.

In this paper, we will utilize two inverse methods: NO and TO methods to solve the inverse problem. In the NO method, we define the material property nodally in the discretized domain and optimize every nodal shear modulus in the inverse scheme. In the TO method, we assume the material property merely varies along the thickness. Thus, fewer optimization variables are required in this inverse scheme. For instance, for a cubic domain discretized by $100 \times 100 \times 100$ nodes, the total number of optimization variables in the NO method is 10^6, while in the TO method, the total number of optimization variables reduces to 100.

2.2.3. Adjoint method

For the NO method, the gradient of Eq. (2) with respect to the nodal shear modulus μ_i is:

$$\frac{\partial J}{\partial \mu_i} = \left\langle (u - u_{\text{meas}}),\ \frac{\partial u}{\partial \mu_i} \right\rangle + \frac{\alpha}{2}\int_\Omega \frac{\nabla\mu_i \frac{\partial(\nabla\mu_i)}{\partial\mu_i}}{\sqrt{(\nabla\mu_i)^2 + c_0{}^2}}\ d\Omega \tag{3}$$

where $\langle u, v\rangle$ is the inner product operator defined by $\int u \cdot v\ d\Omega$; $\frac{\partial u}{\partial \mu_i}$ can be solved by the finite element forward problem:

$$\begin{aligned} \mathrm{K}u &= F \\ \frac{\partial u}{\partial \mu_i} &= -K^{-1}\frac{\partial K}{\partial \mu_i}u \end{aligned} \tag{4}$$

In the equation above, $\mathbf{K}$ is the global stiffness matrix, $\mathbf{F}$ is the force vector.

Substituting Eq. (4) into Eq. (3), we obtain:

$$\begin{aligned} \frac{\partial J}{\partial \mu_i} &= \left\langle (u - u_{\text{meas}}),\ -K^{-1}\frac{\partial K}{\partial \mu_i}u \right\rangle + \frac{\alpha}{2}\int_\Omega \frac{\nabla\mu_i \frac{\partial(\nabla\mu_i)}{\partial\mu_i}}{\sqrt{(\nabla\mu_i)^2 + c_0{}^2}}\ d\Omega \\ &= \left\langle -K^{-\mathrm{T}}(u - u_{\text{meas}}),\ \frac{\partial K}{\partial \mu_i}u \right\rangle + \frac{\alpha}{2}\int_\Omega \frac{\nabla\mu_i \frac{\partial(\nabla\mu_i)}{\partial\mu_i}}{\sqrt{(\nabla\mu_i)^2 + c_0{}^2}}\ d\Omega \end{aligned} \tag{5}$$

Then we can define $\mathbf{K}^{\mathrm{T}}\mathbf{Q} = -(\mathbf{u} - \mathbf{u}_{\text{meas}})$, where $\mathbf{Q}$ can be obtained by solving the dual problem, Eq. (5) can be further simplified as:

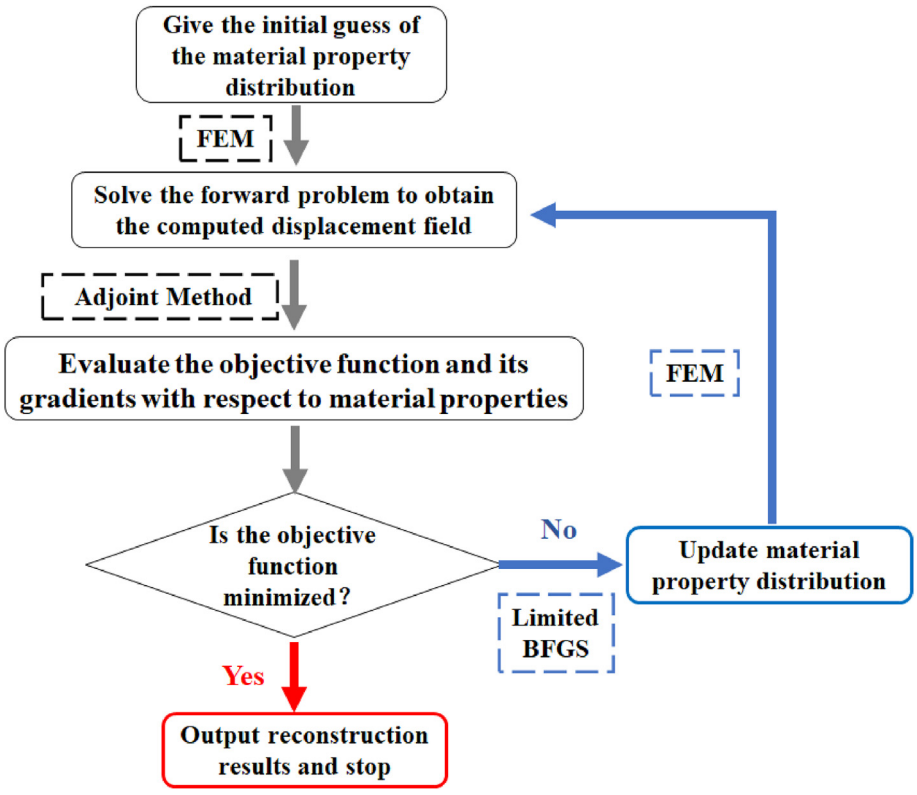

Fig. 3. Flowchart of the inverse algorithm.

$$\frac{\partial J}{\partial \mu_i} = \left\langle Q, \quad \frac{\partial K}{\partial \mu_i} u \right\rangle + \frac{\alpha}{2} \int_{\Omega} \frac{\nabla \mu_i \frac{\partial (\nabla \mu_i)}{\partial \mu_i}}{\sqrt{(\nabla \mu_i)^2 + c_0^2}} \, d\Omega \tag{6}$$

Hence, the gradient of the objective function with respect to the nodal shear moduli can be solved by merely solving the forward problem twice in each minimization iteration. The flowchart of the inverse algorithm is presented in Fig. 3. A similar approach can be applied to the TO method, thus we will skip the discussion.

2.2.4. *Generation of the full-field simulated displacement field*

To test the performance of the proposed approaches, we will solve the inverse problem with simulated data generated by the finite element simulation. To mimic the real measurement, we add up to 3% white Gaussian noise into the full-field simulated data. The noise level is defined as follows:

$$\varepsilon = \sqrt{\frac{\sum_{i=1}^{N} \left(u_i^{noise} - u_i\right)^2}{\sum_{i=1}^{N} \left(u_i\right)^2}} \times 100\% \tag{7}$$

where N is the total number of FE nodes; u_i^{noise} and u_i are the noise displacement and accurate displacement of the i-th node, respectively.

To quantitatively analyze the reconstruction results, we define the relative error of the reconstructed shear modulus:

$$e = \sqrt{\frac{\sum_{k=1}^{S} \left(\mu_k - \mu_k^{target}\right)^2}{\sum_{k=1}^{S} \left(\mu_k^{target}\right)^2}} \times 100\% \tag{8}$$

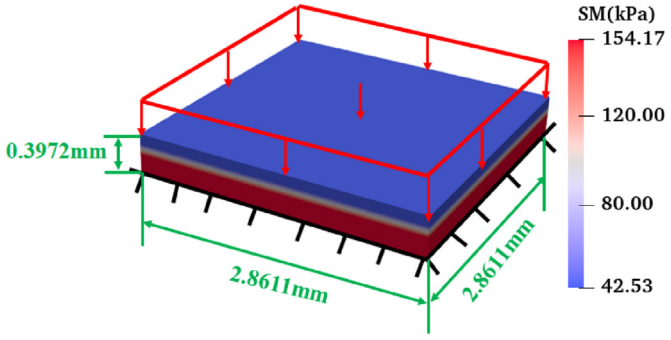

Fig. 4. The target shear modulus distribution and the boundary conditions of the domain of interest.

where S is the total number of FE nodes in the domain of interest; μ_k and μ_k^{target} are the reconstructed shear modulus and target shear modulus of the k-th node, respectively.

3. Results

3.1. Simulated data

In this case, we consider a 3D cuboid with the dimension 2.8611 × 2.8611 × 0.3972 mm^3. The cuboid specimen consists of two layers and is discretized by 1280 tetrahedral elements as shown in Fig. 4. For each layer, we assume it is homogeneous. The target shear moduli of the upper and lower layers are 42.53 kPa and 154.17 kPa, respectively [10]. To avoid the rigid body motion, we fix the bottom face of the specimen and apply uniform pressure on the upper face.

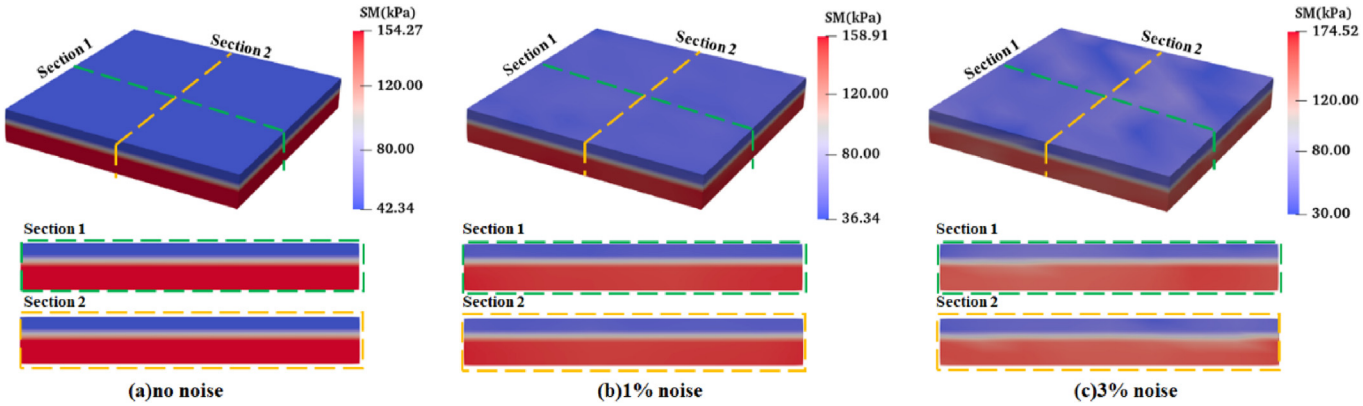

Fig. 5. Reconstructed results acquired by the NO method with varying noise levels. (a) 0% noise; (b) 1% noise; (c) 3% noise.

Fig. 5 presents the reconstructed results by the NO method with full-field simulated displacement data with different noise levels. The reconstructed results show that the NO method performs well even in the presence of 3% noise. Specifically, the interface between the two layers is well preserved. In Table 1, we calculate the relative error of shear modulus in the entire problem domain. We observe that with the increase of the noise level, the error between the reconstructed shear modulus and the target shear modulus increases.

Fig. 6 shows the reconstructed results by the TO method with full-field simulated displacement data. The reconstructed results show that even with 3% noise, the shear moduli of each layer are almost close to the target shear modulus distribution, and the interface between two layers is well reconstructed. Similar to the NO method, the TO method performs worse with the increase of the noise level. However, compared with the NO method, the error between the reconstructed shear modulus and the target shear modulus is smaller as shown in Table 1. The maximum error for the case with 3% noise is roughly 2%. In addition, we also report the computational time of each numerical example of the NO and TO methods in Table 2. Table 2 indicates that the TO method is computationally faster than the NO method since fewer optimization variables are involved in the TO method.

Table 1
Relative error of the reconstructed shear modulus for TO and NO methods.

Method	Noise Level		
	No noise	1% noise	3% noise
NO	0.087%	1.61%	5.55%
TO	5.27×10^{-4}%	0.23%	2.08%

Table 2
Total operation time of reconstructed shear modulus for two methods.

Method	Noise Level		
	No noise	1% noise	3% noise
NO	56495s	1025s	1393s
TO	250s	247s	222s

Next, we evaluate the sensitivity of the identified shear moduli to the initial guess values. We select the noise-free full-field displacement data of the simulated data for inversion. We assume that the solid is homogenous initially with the shear moduli of 50 kPa, 100 kPa, and 200 kPa. It seems that the initial guesses do not affect the reconstructed shear modulus distributions as shown in Fig. 7. Moreover, Table 3 shows the relative error of the shear moduli from the TO method is roughly 1000 times less than that from the NO method. This demonstrates that the TO method is less sensitive to the initial guess.

3.2. Experimental data from OCT

In order to verify the feasibility of the proposed inverse algorithms, we utilize a set of the experimental data acquired from OCT. The

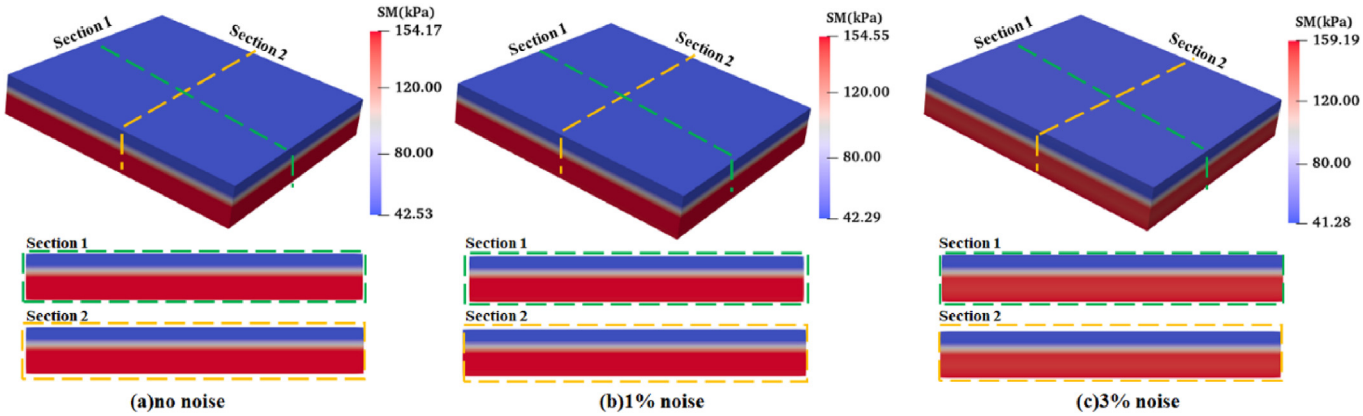

Fig. 6. Reconstructed results acquired by the TO method with varying noise levels. (a) 0% noise; (b) 1% noise; (c) 3% noise.

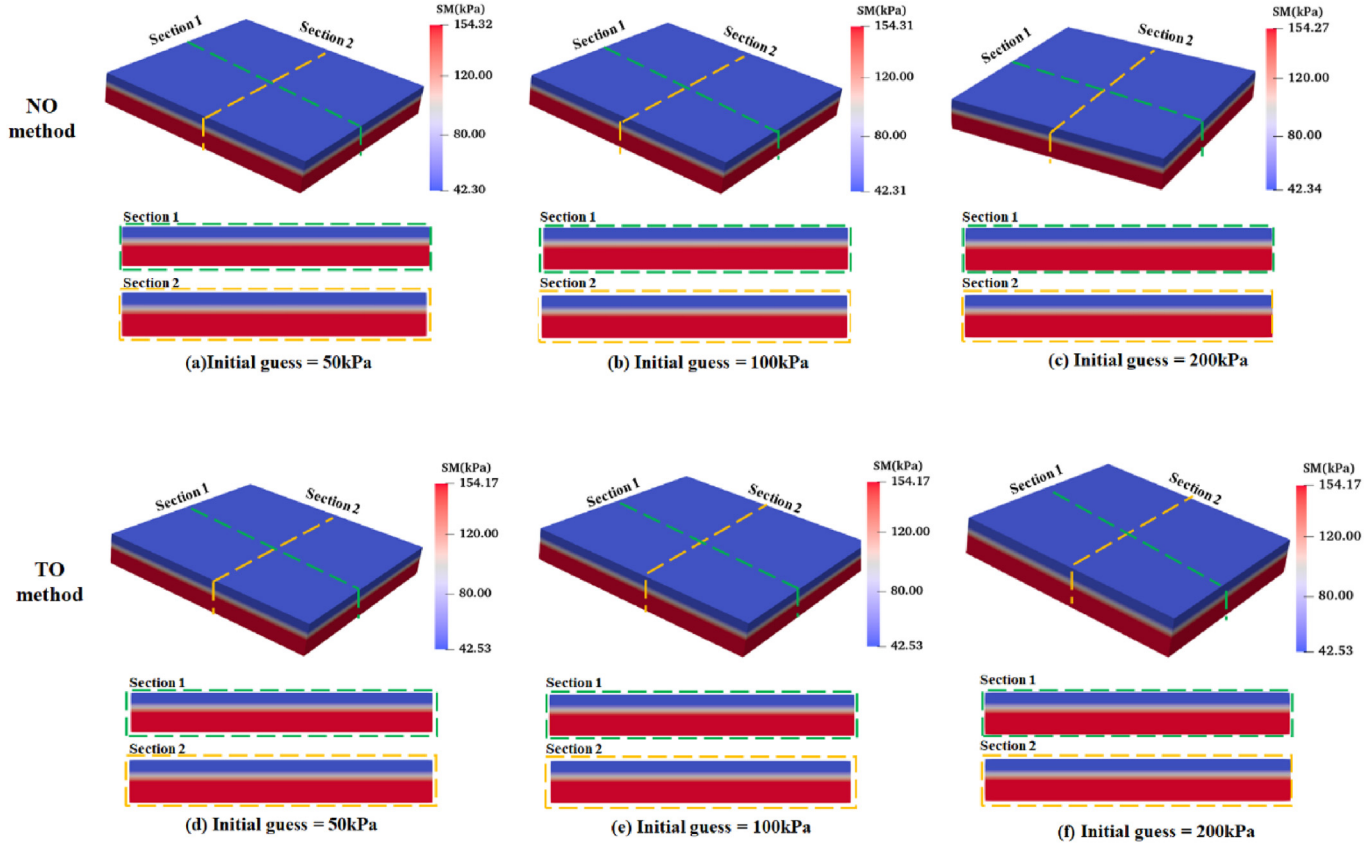

Fig. 7. Reconstructed results acquired by the two methods with varying initial guess of the shear modulus distribution. (a–c) Reconstructed results acquired by the NO method with initial guess values 50 kPa, 100 kPa, and 200 kPa, respectively. (d–f) Reconstructed results acquired by the TO method with initial guess values 50 kPa, 100 kPa, and 200 kPa, respectively.

Table 3
Relative error of identified shear moduli in Fig. 7

Method	Initial Guess		
	50 kPa	100 kPa	200 kPa
NO method	0.109%	0.104%	0.087%
TO method	5.269×10^{-4}%	5.269×10^{-4}%	5.269×10^{-4}%

measured displacement components in all three directions are shown in Fig. 8. In this paper, we merely reconstruct a part of the entire specimen which is depicted by the blue line in Fig. 8(a). Thereby, we solve the inverse problem utilizing the full-field displacement measurement of the domain within the blue line. However, we observe that the measurements within green lines in Fig. 9(a) are noisy, thus we neglect the measured data within green lines and utilize the measurement in the rest part to solve the inverse problem (we will call this "partial region data" for convenience in the following). Moreover, since the measurement along the loading direction is usually more accurate than the measurement in the lateral direction, we will also solve the inverse problem merely using the z displacement component.

The reconstructed results using the NO method are shown in Fig. 10. According to the shear modulus reconstruction, we can clearly visualize the two layers using full-field measurement. However, the quality of the shear modulus reconstruction is low as the upper left and right parts are not well recovered. Besides, there are artifacts appearing on the lower part. If we use the partial region data to solve the inverse problem again, the quality of shear modulus distribution of the upper left and right parts improves slightly. If we only utilize the z displacement component to solve the inverse problem, we observe that the quality of the reconstruction improves significantly. That is, the artifact on the bottom disappears, and the interface between two layers is recovered much better than the other cases. Additionally, the reconstructed shear moduli are of the same order of magnitude as that reported in the reference [10].

The reconstructed results using the TO method are shown in Fig. 11, and we observe that both the full-measured and partial datasets yield better reconstruction results. The ratio of the estimated shear moduli between the upper and lower layers is 0.276 in the reference [10], and the reconstructed results of different measured datasets by the proposed methods are reported in Table 4.

4. Discussion

In this paper, we perform a comparative study on the OCE using both the full-field and partial displacement measurements. Both the simulated and experimental datasets for bilayer soft solids are adopted. We also propose two optimization methods to solve the inverse problem in elasticity. The NO method is the most general way to characterize the shear modulus distribution of solids. Taking advantage of the

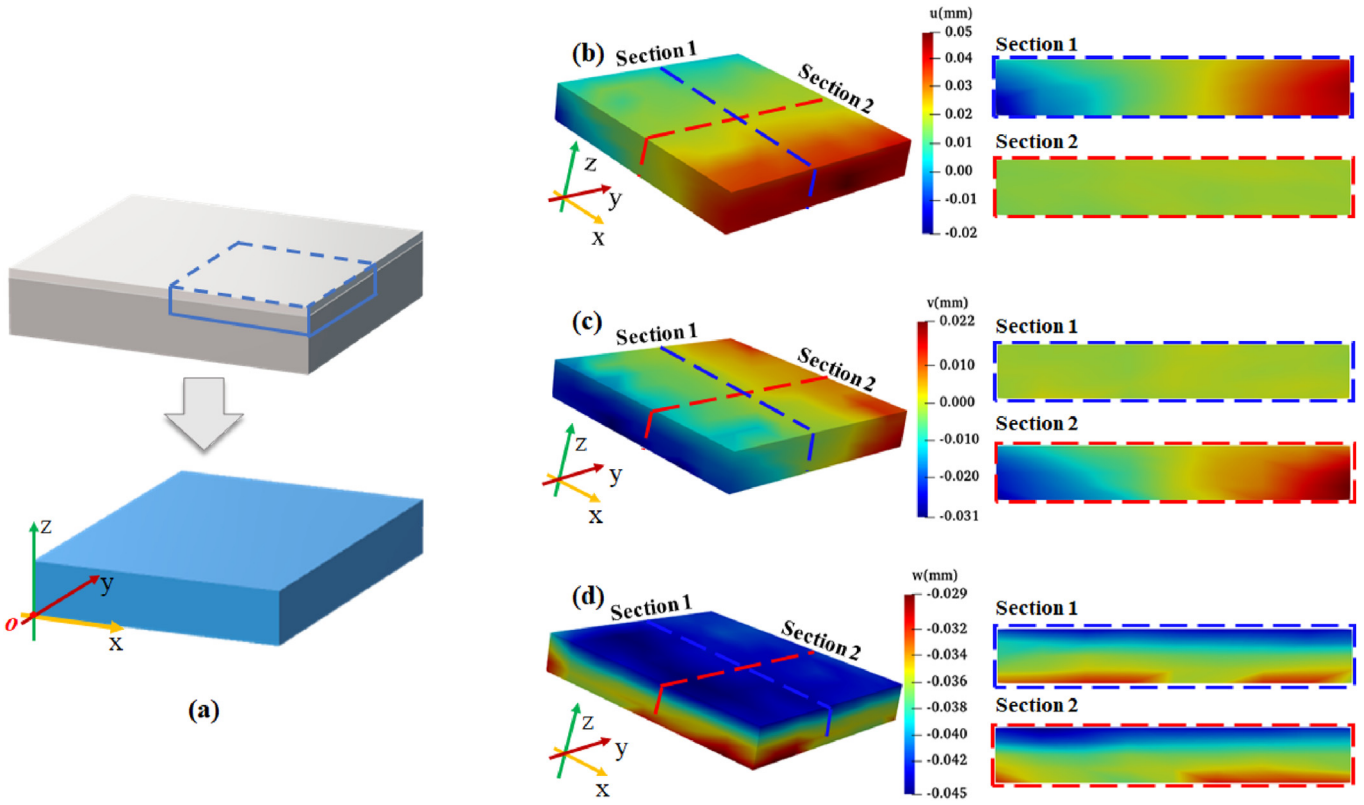

Fig. 8. Displacement measurement. (a) In the blue box are the dimensions of the displacement measurement area and the origin of the coordinate axis; (b–d) The measured displacement component in *x*, *y* and *z* directions, respectively. And the displacement distributions of the section of interest are marked within the red and blue dotted boxes.

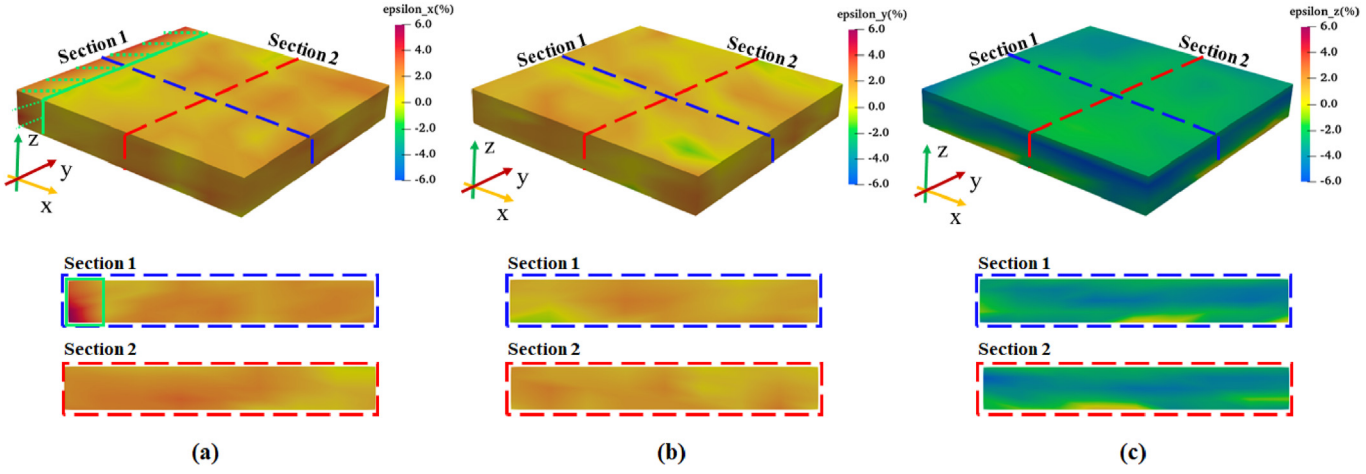

Fig. 9. (a), (b) and (c) are normal strain component in the *x*, *y*, *z* directions, respectively. And the strain distributions along the section of interest are marked within the red and blue dotted boxes.

characteristic of the layered structure, we also propose the TO method that merely reconstructs the shear moduli along the thickness. Since the experimental data is noisy, we also solve the inverse problem in elasticity using partial displacement measurements.

The reconstructed results in this work demonstrate that the TO method yields better reconstruction than the NO method. This observation is intuitive since fewer optimization variables are involved in the TO mothed. Thus, the TO method might be very useful for characterizing the elastic property distribution of layered structures such as skin [18,19] or lamina cribrosa [4,20].

Theoretically speaking, full-field displacement measurement provides more deformation information than partial data. Thus, with the full-field

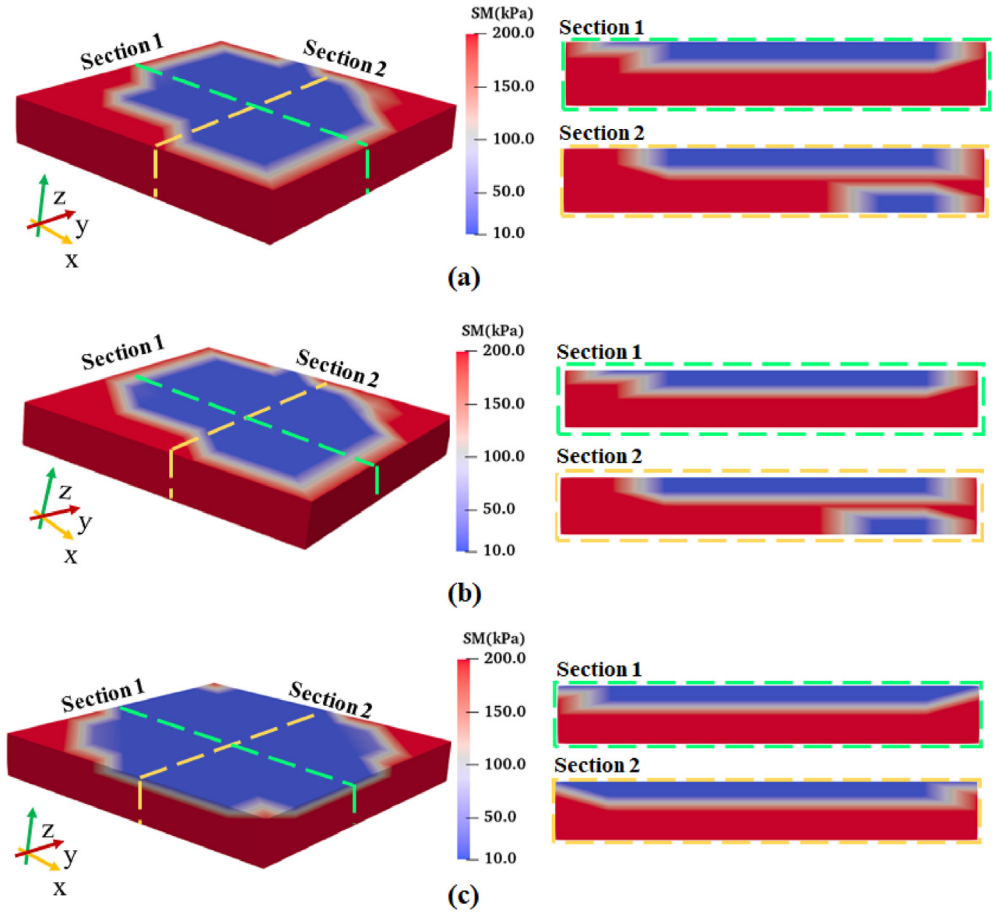

Fig. 10. Reconstructed results of the NO method with different measured datasets. (a) Full-field displacement is utilized, (b) Partial region data is utilized, (c) Only z displacement component is utilized. Two shear modulus maps on the right side of each 3D image are the cross-sections along the dashed lines on (a–c).

displacement measurement, we should obtain better reconstructed results. However, we observed that the reconstructed results using the partial data are better than those that using the full-field displacement. This is probably due to the fact that the full-field displacement measurement is noisy and might be even more noisy at some regions of interest. Thus, it is not necessary to utilize the full-field measurement to acquire accurate elastic property distribution. Additionally, since the displacement component along the loading direction is usually less noisy, thus merely using the displacement component along the loading direction can significantly improve the solution to the inverse problem.

Though the values of the shear moduli obtained by the NO and TO methods are in the same order with those reported in Ref. [10] where VFM is utilized to estimate shear modulus values of the two layers, the relative error between them is still high. Thereby, how to improve the accuracy of the estimation of the shear modulus values at each region with different material properties by the proposed OCE approaches still needs more effort.

5. Conclusion

In this paper, we apply the OCE to characterize the elastic property distribution of bilayer soft solids using both the full-field and partial displacement measurements. We first utilize the simulated data to test the feasibility of the inverse solver utilized in the OCE system. The shear modulus distribution acquired with the simulated data has successfully shown the proof of concept of the inverse solver. We also observe that the TO method has shown a stronger capability of reconstructing shear modulus distribution than the NO method. This observation is also validated by the experimental data from OCT. By comparing the reconstructed shear modulus distributions from the full-field and partial displacement measurements, we also observe that using accurate partial displacement measurement can improve the quality of the shear modulus reconstruction. The results in this paper have great signification in applying OCE into characterizing the elastic property distribution of layered soft tissues such as skin and cornea.

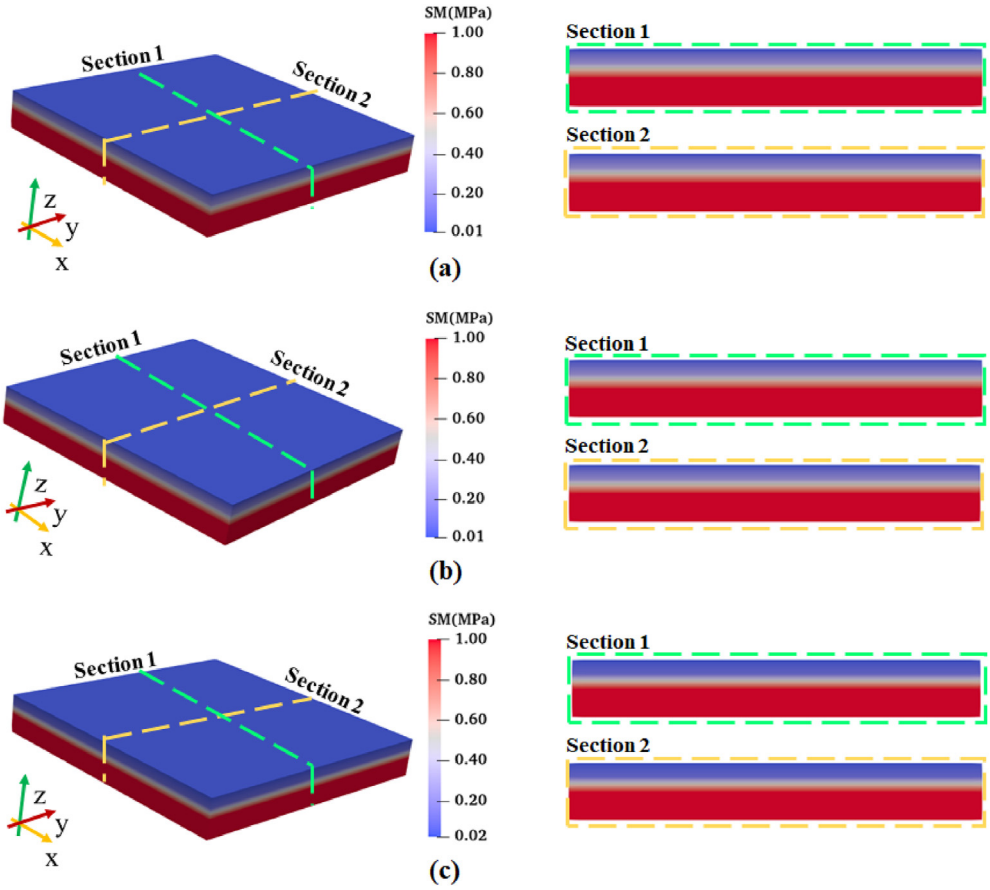

Fig. 11. Reconstructed results of the TO method with different measured datasets. (a) Full-field displacement is utilized, (b) Partial region data is utilized, (c) Only z displacement component is utilized. Two shear modulus maps on the right side of each 3D image are the cross-sections along the dashed lines on (a–c).

Table 4
The ratio of the estimated shear moduli between the upper and lower layers of different measured datasets by TO and NO methods.

Method	Datasets		
	Full-field displacement	Partial region	Only z displacement component
NO	0.812	0.802	0.587
TO	0.130	0.121	0.073

Funding sources

The authors acknowledge the support from the National Natural Science Foundation of China (12002075, 11732004, 12021002), the National Key Research and Development Plan (2020YFB1709401), the Foundation for Innovative Research Groups of the National Natural Science Foundation (11821202), the Natural Science Foundation of Liaoning Province in China(2021-MS-128).

Author contribution to study

Dongmei Zhao: Data curation, Writing and Original draft preparation. L Haosen Wang: Experiments. Jianwei Deng: Simulation. IrynaSlavashevich:Reviewing and Editing. Xu Guo: Investigation, Reviewing and Editing. Yue Mei: Conceptualization, Methodology, Reviewing and Editing. Cuiru Sun: Conceptualization, Reviewing and Editing.

Declaration of competing interest

The authors declare that there are no conflicts of interest.

References

[1] Chang JM, Moon WK, Cho N, et al. Clinical application of shear wave elastography (SWE) in the diagnosis of benign and malignant breast diseases. Breast Cancer Res Treat 2011;129:89–97. https://doi.org/10.1007/s10549-011-1627-7.
[2] Sandrin L, Fourquet B, Hasquenoph JM, et al. Transient elastography: a new noninvasive method for assessment of hepatic fibrosis. Ultrasound Med Biol 2003; 29:1705–13. https://doi.org/10.1016/j.ultrasmedbio.2003.07.001.
[3] Skovorda AR, Klishko AN, Gusakian DA, et al. Quantitative analysis of mechanical characteristics of pathologically altered soft biological tissues. Biofizika 1995;40: 1335–40.
[4] Zhang L, Beotra MR, Baskaran M, et al. In vivo measurements of Prelamina and Lamina Cribrosa biomechanical properties in humans. Investig Ophthalmol Vis Sci 2020;61:27. https://doi.org/10.1167/iovs.61.3.27.
[5] Pham T, Sun W. Material properties of aged human mitral valve leaflets. J Biomed Mater Res 2014;102:2692–703. https://doi.org/10.1002/jbm.a.34939.
[6] Patil AV, Krouskop TA, Ophir J, et al. On the differences between two-dimensional and three-dimensional simulations for assessing elastographic image quality: a simulation study. Ultrasound Med Biol 2008;34:1129–38. https://doi.org/10.1016/j.ultrasmedbio.2007.12.007.
[7] Johnson CL, McGarry MDJ, Van Houten EEW, et al. Magnetic resonance elastography of the brain using multishot spiral readouts with self-navigated motion correction. Magn Reson Med 2013;70:404–12. https://doi.org/10.1002/mrm.24473.
[8] Dong L, Wijesinghe P, Dantuono JT, et al. Quantitative compression optical coherence elastography as an inverse elasticity problem. IEEE J Sel Top Quant Electron 2015;22:277–87. https://doi.org/10.1109/JSTQE.2015.2512597.
[9] Dong L, Wijesinghe P, Sampson DD, et al. Volumetric quantitative optical coherence elastography with an iterative inversion method. Biomed Opt Express 2019;10: 384–98. https://doi.org/10.1364/BOE.10.000384.
[10] Meng F, Zhang X, Wang J, et al. 3D strain and elasticity measurement of layered biomaterials by optical coherence elastography based on digital volume correlation

and virtual fields method. Appl Sci 2019;9:1349. https://doi.org/10.3390/app9071349.
[11] Oberai AA, Gokhale NH, Feijóo GR. Solution of inverse problems in elasticity imaging using the adjoint method. Inverse Probl 2003;19:297. https://doi.org/10.1088/0266-5611/19/2/304.
[12] Liu Z, Sun Y, Deng J, et al. A comparative study of direct and iterative inversion approaches to determine the spatial shear modulus distribution of elastic solids. Int J Appl Mech 2019;11:1950097. https://doi.org/10.1142/S1758825119500972.
[13] Sridhar SL, Mei Y, Goenezen S. Improving the sensitivity to map nonlinear parameters for hyperelastic problems. Comput Methods Appl Mech Eng 2018;331:474–91. https://doi.org/10.1016/j.cma.2017.11.028.
[14] Mei Y, Goenezen S. Mapping the viscoelastic behavior of soft solids from time harmonic motion. J Appl Mech 2018;85:041003. https://doi.org/10.1115/1.4038966.
[15] Boppart SA, Bouma BE, Brezinski ME, et al. Imaging developing neural morphology using optical coherence tomography. J Neurosci Methods 1996;70:65–72. https://doi.org/10.1016/S0165-0270(96)00104-5.
[16] Mei Y, Tajderi M, Goenezen S. Regularizing biomechanical maps for partially known material properties. Int J Appl Mech 2017;9:1750020. https://doi.org/10.1142/S175882511750020X.
[17] Zhu C, Byrd RH, Lu P, et al. Algorithm 778: L-BFGS-B: fortran subroutines for large-scale bound-constrained optimization. ACM Trans Math Software 1997;23:550–60. https://doi.org/10.1145/279232.279236.
[18] Liu X, Chuchvara N, Liu Y, et al. Real-time deep learning assisted skin layer delineation in dermal optical coherence tomography. OSA Continuum 2021;4:2008–23. https://doi.org/10.1364/OSAC.426962.
[19] Hussein S. Automatic layer segmentation in H&E images of mice skin based on colour deconvolution and fuzzy C-mean clustering. Inform Med Unlocked 2021;25:100692. https://doi.org/10.1016/j.imu.2021.100692.
[20] Kim TW, Lee EJ. Lamina cribrosa imaging. In: Park Ki Ho, Kim Tae-Woo, editors. OCT imaging in glaucoma. Singapore: Springer Inc; 2021. p. 55–70.